Complex impedance, dielectric properties and electrical conduction mechanism of La0.5Ba0.5FeO3-delta perovskite oxides

RSC Advances

This article can be cited before page numbers have been issued, to do this please use: S. Nasri, A. L. Ben Hafsia, M. Tabellout and M. Megdiche, *RSC Adv.*, 2016, DOI: 10.1039/C6RA10589K.

ROYAL SOCIETY OF CHEMISTRY

www.rsc.org/advances

View Article Online
DOI: 10.1039/C6RA10589K

Complex impedance, dielectric properties and electrical conduction mechanism of $La_{0.5}Ba_{0.5}FeO_{3-\delta}$ perovskite oxides

S.Nasri *[1], A. L. Ben Hafsia [2, 3], M .Tabellout [4] M.Megdiche [1]

[1] Condensed Matter Laboratory, University of Sfax, Faculty of Sciences, Tunisia

[2] Laboratoire de chimie inorganique, Faculté des sciences de Sfax, Tunisia.

[3] EMAT, University of Antwerp Groenenborgerlan 171, B-2020 Antwerp, Belgium

[4] Institut des Molécules et Matériaux du Mans, IMMM UMR CNRS 6283, Université du Maine, Avenue Olivier Messiaen, 72085 Le Mans Cedex 9, France.

*: Corresponding author:

nasri.saber.1@gmail.com

Abstract:

The new perovskite compound $La_{0.5}Ba_{0.5}FeO_{3-\delta}$ was prepared by the sol-gel method. The Rietveld refinement, from the X-ray diffraction pattern, proofed that the sample presents single phase type cubic structure at room temperature. In addition, Electrical properties were performed using complex impedance spectroscopy (CIS) technique as a function of frequency (100 Hz-7 MHz) at various temperatures (278-573 K). As a matter of fact, impedance analysis was performed using the equivalent circuit model and it indicated the presence of a single semicircle arc. Furthermore, the obtained results of the AC conductivity have been discussed in terms of non-overlapping small polaron tunneling (NSPT) model. Finally, it is worth to mention, that the conductivity of our investigated perovskite oxide was found to be σ_{573}= $1.23*10^{-2}$ $\Omega^{-1}cm^{-1}$. These results confer to this material a potential application as cathode materials.

Keywords: Perovskite oxide, Complex impedance, AC conductivity, Conduction Mechanism, NSPT model

View Article Online
DOI: 10.1039/C6RA10589K

1. INTRODUCTION

In recent years, the perovskite type structures with the general formula ABO_3 are the most intensely investigated materials in chemistry and physics **[1]**. In fact, these materials show several interesting physical and chemical properties; they can have different electronic behavior from insulating to metallic, with spin-polarized electrical conductivity**[2,3]**, and they can have ferroic atomic displacements **[4]**, mixed ionic and electronic conducting (MIEC) properties **[5]** and catalytic properties **[6]**. Moreover, perovskite oxide can combine many of these properties simultaneously, allowing for new properties, such as multiferroicity **[7]**. As a result, the perovskite type materials have also an important technological interest, with various industrial possible applications such as dielectrics or piezoelectrics in electronic devices and sensors **[1]**, magnetic memory components **[3]**, electrode and electrolyte materials for fuel cells (SOFC) cathode **[8]**, and components for solar cells **[9]**. On the other hand, the easy manufacturing, low cost and the interesting magnetic and electric properties, lead this type of materials to be one of the important ceramics that has attracted a considerable attention in the field of technological applications extended from microwave to radio frequency **[10, 11]**.

As a matter of fact, most of the substitution studies of these perovskite type structures (ABO_3) were focused on the A-site and researchers were widely investigating the effect of these substitutions in the LBMO system ($LaBaMnO_3$). In contrast, only very few and rare studies have attempted to study the effect of the substitutions at the Mn-site [12]. As it is well established, the Mn plays an important role in transport properties and the doping in B-sites leads to change the electrical behavior of the material. It is hence worth to investigate the influence of doping by other ions at the Mn-site. In these last years, iron (Fe) appears as an interesting choice of dopant ions as the ionic radii of Mn^{3+} and Fe^{3+} are too close.

In a previous study by Rahmouni, only the effect of very low percentages of doping iron in the Ac conductivity has been studied and a model of conduction was suggested [13]. Furthermore, previous studies of $BaLaFe_2O_{5.91,}$ Battle et al. [14] and K. S. Roh et al [15] suggested that the crystal system is cubic and the space group is Pm-3m, but no dielectric measurement has been investigated. Based on the above discussed points, we have been interested to study the behavior of AC conductivity and dielectric properties of higher concentration of baruim doped at A-site in $La_{0.5}Ba_{0.5}FeO_{3-\delta}$ at different frequencies and temperatures. Thus, the sample was analyzed by scanning electron microscopy, X-ray diffraction, and electrochemical impedance spectroscopy. Moreover, light has been shed on

View Article Online
DOI: 10.1039/C6RA10589K

the investigation of the AC conduction process. Consequently, a detailed study of the electric transport behavior was made. As a result, the conduction mechanism was analyzed using non small polaron hopping model (NSPT). The related parameters are discussed and reported herein.

2. Materials and Methods

$La_{0.5}Ba_{0.5}FeO_{3-\delta}$ powder was synthesized by sol-gel method. In a typical procedure, we have been using stoichiometric amounts of $La(NO_3)_2.H_2O$; $Ba(NO_3)_2$; $Fe(NO_3)_3$. The precursors were dissolved into deionized water, and adding ethylene glycol and citric acid. The solution was kept at 150 °C for 2h, and was then heated at 600°C for 6h. Finally, the obtained powder was fired respectively at 1100 °C, 1300 °C for 12h (it was crushed in an agate mortar in between). At room temperature, the structure and phase purity of the prepared sample were determined by X-ray powder diffraction (PHILIPS diffractometer, X'PERT PRO) using Cu K_α ($\lambda_1 = 1.5405$ Å; $\lambda_2 = 1.5444$ Å) radiation with a step size of $\Delta 2\theta = 0.017°$ between $2\theta = 15°$ and 85°. The lattice parameters of the synthesized powder were determined from powder X-ray diffractograms by employing the Rietveld method and the FULLPROF program**[16]**. Indeed, the surface morphology of the investigated sample was examined using an Environmental Scanning Electron Microscopy (JEOL, JSM 650 LV).

For the electrical characterizations, the measurements were performed using NOVOCONTROL system integrating ALFA dielectric interface over a frequency range from 100 Hz to 7 MHz at various temperatures (278 -573 K).

3. RESULTS AND DISCUSSION

3.1 Structural characterization

X-ray diffraction pattern of the LBFO compound is shown in **Fig. 1**. In fact, the sample showed a pure perovskite structure (ABO_3) without any secondary phases. As observed from **Fig. 1**, all the reflection lines were indexed to cubic structure with *Pm-3m* space group. The lattice parameter is 3.93843 Å as determined from the Rietveld refinement. The conventional reliability factors were $\chi^2 = 1.43$, $R_f = 1.69$ and Bragg factor $R_B = 1.84$.

The morphology and particle size of $La_{0.5}Ba_{0.5}FeO_{3-\delta}$ observed by SEM is shown in Fig.1 (inset). It is clearly seen that the particles are agglomerated with an average particle size, found from the size distribution, of 63 nm. Also we can calculate the average crystallite size (D) from XRD peaks using the Scherer formula:

$$D = 0.9\,(\lambda/\beta \cos\theta) \qquad (1)$$

View Article Online
DOI: 10.1039/C6RA10589K

Where λ is the X-ray wavelength, θ is the diffraction angle for the most intense peak (101), and β is defined as $\beta^2 = \beta^2_m - \beta^2_s$. Here β_m is the experimental full width at half maximum (FWHM) and β_s is the FWHM of a standard silicon sample [17]. The calculate crystallite size (D) obtained from our XRD pattern is 65.5 nm for our sample. Thus the size observed by SEM is comparable to the particle size obtained from the XRD data.

3.2 Impedance analysis

The electrical properties of the perovskite LBFO compound were investigated by using a complex impedance spectroscopy technique. This technique is particularly useful for the characterization of electrical properties of electro-ceramic materials, such as conductivity, dielectric constant, relaxation characteristic, etc.

The complex plane plot of the investigated sample is given in **Fig. 2** at several measurement temperatures. From the figure, one semi-circle arc is clearly observed at all studied temperatures. Considering this, the presence of a single semicircular arc indicates that the electrical processes in the material arise basically due to the contribution from grain material. In addition, the decreasing radius of the arcs with increasing temperature suggests the insulating or semiconducting nature of the perovskite LBFO**[18]**.

In order to more clearly understand the relaxation process, the Nyquist plots were fitted using Z-view software. The best fits are obtained when we use an equivalent circuit involving a parallel combination of a resistance, capacitance, and fractal capacitance (**Fig. 2 inset**). The impedance of CPE is given by the relationship:

$$Z_{CPE} = \frac{1}{Q(j\omega)^{\alpha}} \tag{2}$$

Where α is related to the deviation from the vertical of the line in the –Z″ versus Z′ plot.

α= 1 indicates a perfect capacitance and lower α values directly reflect the roughness of the electrode used. In such condition, the real and imaginary components of the whole impedance are calculated according to the following expressions:

$$Z' = \frac{R_g^2 Q_g \omega \cos(\frac{\alpha_g \pi}{2}) + R_g}{(R_g Q_g \omega^{\alpha_g} \cos(\frac{\alpha_g \pi}{2}) + 1)^2 + (R_g Q_g \omega^{\alpha_g} \sin(\frac{\alpha_g \pi}{2}))^2} + \frac{\cos(\frac{\alpha_e \pi}{2})}{Q_e \omega^{\alpha_e}} \tag{3}$$

View Article Online
DOI: 10.1039/C6RA10589K

$$-Z''=\frac{R_g^2 Q_g \omega \sin(\frac{\alpha_g \pi}{2})+R_g}{(R_g Q_g \omega^{\alpha_g}\cos(\frac{\alpha_g \pi}{2})+1)^2+(R_g Q_g \omega^{\alpha_g}\sin(\frac{\alpha_g \pi}{2}))^2}+\frac{\sin(\frac{\alpha_e \pi}{2})}{Q_e \omega^{\alpha_e}} \quad (4)$$

Fig. 3 shows the real Z′ component of the impedance as a function of frequency, at different temperatures. The amplitude of Z′ is higher in the low frequency region and it decreases monotonically with increase in frequency and remains invariant at higher frequencies irrespective of temperature. In addition, the magnitude of Z′ decreases with the rise in temperature (NTCR behavior) and their values for all temperatures merge in the higher frequency region. This trend of Z′ (decrease with rise in temperature and frequency) may be due to increase in ac conductivity with temperature and frequency.

The decrease of Z′ is up to a certain frequency and then it remains almost constant with the increase in frequency. This may be due to the release of space charge polarization as a result of the lowering of the barrier properties of the materials at higher temperatures in this material**[19]**. This particular frequency at which Z' value becomes independent of frequency is found to shift toward the higher frequency side with rise in temperature indicating the possibility of frequency relaxation process in the material **[20, 21]**. The same phenomenon of Z' has already been observed in many other perovskite materials **[22].**

Fig. 4 shows the frequency dependence of imaginary impedance Z″ at different temperatures for LBFO compound within the measured frequency. As seen from the figure, the Z″ value increases initially, attains a peak Z''_{max} and then decreases with frequency as well as temperature. It is worth noting that the average peak position regularly shifts to higher frequency with increasing temperature which suggests a spread of relaxation time in the system **[23]**.Thus; the merger of all the curves at high frequencies indicates a possible release of space charge.

Fig. 5 depicts the frequency dependence of Z′ and Z″ fits to the equivalent circuit and their corresponding Argand diagram (inset figure) drawn at 293 K. It is worth to mention, that those spectra clearly show a good agreement between theoretical and experimental data indicating that the proposed equivalent circuit clearly describes the electrical properties of the sample.

The electrical conductivity is calculated as follows: $\sigma_{dc}=\frac{e}{R*S}$ where e is the electrolyte-electrode contact area and s is the sample thickness. **Fig. 6** shows the thermal evolution of the

View Article Online
DOI: 10.1039/C6RA10589K

conductivity dc Ln (σ_{dc}*T) versus 1000/T. It can be seen that the conductivity versus temperature response satisfies a linear dependence governed by the Arrhenius law:

$$\sigma_{dc}T=Aexp(\frac{-E_a}{k_B T}) \quad (5)$$

Where σ_{dc} is the dc conductivity, A is the pre-exponential factor, T is the temperature, E_a is the dc conductivity activation energy and k_B is the Boltzmann's constant. The calculated activation energy of the conduction corresponding to the grain was found to be 0.39 eV (see **Fig.6**).

3.3 Electric modulus studies

The electric modulus was basically introduced by Macedo et al. **[24]** to study the space charge relaxation phenomena. From the physical point of view, this formalism provides deep insights into charge transport processes such as mechanism of conductivity relaxation and ion dynamics as a function of frequency and temperature. In fact, the electric modulus is calculated from the impedance data using the relation:

$$M^*= \omega C_o Z^* \quad (6)$$

Here C_0 is the vacuum capacitance of the cell.

Fig. 7 shows the variation of the real part of the electric modulus M′ as a function of frequency over a range of temperature. As seen from **Fig. 7**, the value of M′ is very small in the low frequency region. This behavior can be interpreted by a lack of restoring force which governs the mobility of charge carriers under the influence of an electric field **[25]**. Otherwise, an increase in the value of M′ with increasing frequency at different temperatures has been observed.

Shown in **Fig. 8** is the variation of imaginary part M″ with frequency at different temperatures. Thus, at different temperature, M ″ increase with frequency up to a maximum peak, M''_{max}, then decrease. On the other hand, the position of the relaxation peak shifts towards higher frequency with increasing temperature. This is indicative of temperature dependent relaxation process in the presently studied sample. The frequency region below the M″ peak indicates the frequency range in which polarons drift to long distances and in the frequency range above the peak, the polarons are confined to potential wells and free to move within the wells. Hence, the peak frequency represents the transition from long range to short range mobility.

Following, such dielectric relaxation process, in general, can be interpreted by the numerical Laplace transform of the Kohlraush–Williams–Watts (KWW) decay function, φ(t)=exp[-

View Article Online
DOI: 10.1039/C6RA10589K

$(t/\tau)^{\beta}]$, where the exponent β characterizes the degree of non-Debye behavior and τ is the conductivity relaxation time **[26].** Recently, Bergman has modified the KWW function fitting approach, allowing direct analysis in the frequency domain **[27]**. The imaginary part of the M″ (ω) has been approximated as:

$$M''(\omega) = \frac{M''_{max}}{\left((1-\beta)+\left(\frac{\beta}{(1-\beta)}\right)\right)\left[\beta\left(\frac{\omega_{max}}{\left(\omega+\frac{\omega}{\omega_{max}}\right)^{\beta}}\right)\right]} \quad (7)$$

In equations 6, M''_{max} is the peak maximum of the imaginary part of the modulus and $\omega_{max} = (1/\tau_{max})$ is the peak frequency of the imaginary part of the modulus. Here, experimental data are fitted using this modified KWW approach.

For further study, the temperature variation of the relaxation time ($\tau_{max}=(\omega_{max})^{-1}$ at maximum of M″ is shown in **Fig. 9**, which satisfies the Arrhenius law. Consequently, the estimated value of the activation energy of electric modulus is about 0.30 eV.

3.5 AC conductivity study

The AC electrical conductivity was obtained in accordance with the relation:

$$\sigma_{ac}=\left(\frac{e}{s}\right)\left(\frac{Z'}{Z'^2+Z''^2}\right) \quad (8)$$

Where Z′ and Z″ are, the real and the imaginary part of complex impedance, e and s are the thickness and the area, respectively, of the present pellet.

The frequency dependence ac electrical conductivity of the $La_{0.5}Ba_{0.5}FeO_{3-\delta}$ compound at different temperatures is illustrated in **Fig. 10**. Again, by looking at this figure, it is clear that, this behavior is particularly composed of two parts: A frequency independent part in the low frequency region (as shown by the plateau at low frequencies), followed by a sharp increase at high frequencies. Usually, the phenomenon of the conductivity dispersion is analyzed by the Jonscher power law given as follows **[28]**:

$$\sigma_{ac}(\omega)=\sigma_{dc}+A\omega^{S} \quad (9)$$

In this expression, σ_{dc} is the frequency independent conductivity that is related to dc conductivity, A is the temperature dependent pre-exponential factor and the exponent ***s*** represents the degree of interaction between mobile ions and its surrounding lattices, where $0 < \boldsymbol{s} < 1$.

View Article Online
DOI: 10.1039/C6RA10589K

Fig. 11 shows the variation of dc conductivity with inverse of absolute temperature. In fact, this plot has a linear response and can be explained by a thermally activated transport of Arrhenius type governed by the relation in equation below:

$$\sigma_{dc}T=\sigma_0 \exp(-E_a/kT) \quad (10)$$

where σ_0, E_a and k_B represent the pre-exponential factor, the activation energy of the mobile charge carriers and Boltzmann constant respectively. Indeed, the activation energy obtained from the slope of the straight line was found to be 0.36 eV (see **Fig. 11**). Therefore, the Jonscher fitting parameters are given in **Table 1**.

As it was mentioned earlier, the measurement of ac response of perovskite materials has been extensively used to understand the conduction process **[29]** and it is also a powerful tool for obtaining important information concerning the microscopic charge transport mechanism**[30]**. There have been various theories proposed on the ac response of materials to correlate the conduction mechanism of ac conductivity with S (T) behavior. In fact, for the system under investigation, the temperature dependence of the frequency exponent S is shown in **Fig. 12**. Hence, it is clear that as the temperature rises, this parameter increases. Consequently, this result suggests that the conductivity mechanism of the sample can be stated to be non-overlapping small polaron tunneling (NSPT)**[31]**. It is pertinent to mention that large numbers of perovskite oxides are known to exhibit small polaron conduction as the obtained result **[32-34]**. More precisely, the entity formed by the ionic carrier associated with the polarization as a result of its presence is called polaron. We note also that, in the effective mass approximation for the electron placed in a continuum polarizable (or deformable) medium, which leads to a so-called large or small polaron. Large polaron wave functions and corresponding lattice distortions spread over many lattice sites. The self-trapping is never complete in the perfect lattice. Due to finite phonons frequencies, ion polarization can follow polaron motion if the motion is sufficiently low. Hence, large polaron with a low kinetic energy propagate through the lattices as free electrons but with an enhanced effective mass.

Indeed, if the distortion around the charge carrier is limited to nearest neighbor ions, it comes of small polaron and the conductivity value while taking into consideration the torque charge carrier/distortion. The mobility is relatively low and strongly dependent on the temperature.

According to this model, the exponent S is evaluated as follow:

$$S=1-\frac{4}{\left[\mathrm{Ln}\left(\frac{1}{\omega\tau_0}\right)-\frac{W_H}{k_B T}\right]} \quad (11)$$

Here, W_H denotes the polaron hopping energy and τ_0 is a characteristic relaxation time.

View Article Online
DOI: 10.1039/C6RA10589K

Obviously, the AC conductivity is given by:

$$\sigma_{ac} = \frac{(\pi e)^2 k_B T \alpha^{-1} \omega \left[N(E_F) \right]^2 R_\omega^4}{12} \quad (12)$$

Whither

$$R_\omega = \frac{1}{2\alpha}\left[\ln\left(\frac{1}{\omega\tau_0}\right) - \frac{1}{k_B T} \right] \quad (13)$$

In equations (**11**) and (**12**), the term α^{-1} is the spatial extension of the polaron, $N(E_F)$ represents the density of defect states, and R_ω is the tunneling distance.

With the purpose of checking the validity of the NSPT model on this perovskite oxides and hence to provide information on the origin of the conduction mechanism in relation with the crystal structure, **Fig. 13** shows the typical plots correlating the ac conductivity as a function of temperature for $La_{0.5}Ba_{0.5}FeO_{3-\delta}$ at different frequencies. As a matter of fact, **Fig. 13** plainly depicts that theoretical curves (lines) are in fair agreement with the experimental results (symbols). The calculated fitting parameters are listed in **Table 2**. It is evident from the **Table 2** that the parameters $N(E_F)$ and α^{-1} increase with frequency, which is in accordance with the literature**[35, 36]**.

4. Conclusion

In summary, the pure-phase $La_{0.5}Ba_{0.5}FeO_{3-\delta}$ perovskite oxide was synthesized by the sol–gel state reaction technique. The impedance properties, the modulus analysis and the AC conductivity have been studied using impedance spectroscopic technique. In fact, the analysis of impedance component allowed determining an equivalent electrical circuit. Besides, the AC conductivity spectra of the investigated compound, follows the Jonscher power law. As a result, the temperature dependency of the exponent S shows that the non-overlapping small polaron tunneling (NSPT) is appropriate to explain the conductivity mechanism of LBFO in the studied temperature range. Indeed, future in-depth transport investigation could shed more light on the conduction mechanisms in this perovskite material with mixed ionic-electronic conductibility (MIEC).

View Article Online
DOI: 10.1039/C6RA10589K

Figure caption

FIG.1: Rietveld-refined XRD profile of $\mathbf{La_{0.5}Ba_{0.5}FeO_{3-\delta}}$ at room temperature**.** The scanning electron micrograph of the sample is shown in the inset.

FIG.2: Nyquist plots as a function of temperature with electrical equivalent circuit (inset).

FIG.3: Variation of real part of the impedance as a function of frequency at various temperatures.

FIG.4: Variation of imaginary part of the impedance as a function of frequency and temperature.

FIG.5: Variation of Z′ and Z″ with angular frequency at 293 K; inset is the Cole–Cole plot at the same temperature.

FIG.6: Variation of (Log σ_{dc}* T) vs (1000/T). Symbols are experimental points and solid line is the straight line fit.

FIG.7: Angular frequency dependence of the real part of the electric modulus at different temperatures.

FIG.8: Frequency dependence of the imaginary part of electric modulus at several temperatures.

FIG.9: The temperature dependence of the characteristic relaxation time.

FIG.10: Variation of AC conductivity of $\mathbf{La_{0.5}Ba_{0.5}FeO_{3-\delta}}$ with frequency and temperature. The solid lines are the best fits to Jonscher power law (Eq.8).

FIG.11: The Arrhenius behavior of dc conductivity.

FIG.12: Temperature dependence of the exponent *s* for $\mathbf{La_{0.5}Ba_{0.5}FeO_{3-\delta}}$.

FIG.13: Plots of ln σ_{AC}. vs. 1000/T at different frequencies for $\mathbf{La_{0.5}Ba_{0.5}FeO_{3-\delta}}$.

View Article Online
DOI: 10.1039/C6RA10589K

Table caption:

Table.1: Values of the dc conductance, the constant (A) and the exponent (S), for $La_{0.5}Ba_{0.5}FeO_{3-\delta}$.

Table.2: Parameters used to NSPT model fitting for $La_{0.5}Ba_{0.5}FeO_{3-\delta}$ at various frequencies.

View Article Online
DOI: 10.1039/C6RA10589K

REFERENCES

[1] AS. Bhalla, R. Guo, R. Roy, Mater. Res. Innov, 2000, 4, 3.

[2] WE. Pickett, DJ. Singh, Phys.Rev.B, 1996, 53, 1146.

[3] K-I. Kobayashi, T. Kimura, H. Sawada, K. Terakura, Y. Tokura, Nature, 1998, 395, 677.

[4] NA. Benedek, CJ. Fennie. J Phys Chem C, 2013, 117, 13339.

[5] Li M, MJ. Pietrowski, RA. De Souza, H. Zhang, IM. Reaney, SN. Cook, et al, Nat Mater , 2014, 13, 31.

[6] H. Tanaka, M. Misono. Curr Opin Solid State Mater Sci, 2001, 5, 381.

[7] S-W. Cheong, M. Mostovoy, Nat.Mater, 2007, 6, 13.

[8] Y-H. Huang, RI. Dass, Z-L. Xing, JB. Goodenough, Chem.Inform, 2006, 312, 254.

[9] MA. Green, A. Ho-Baillie, HJ. Snaith, Nat Photonics, 2014, 8, 506.

[10] Y. K. Atanassova, V. N. Popov, G. G. Bogachev, M. N. Iliev, C. Mitros, V. Psycharis, and M. Pissas, Phys. Rev. B **47**, 1993, 15, 201

[11] A. Benali, M. Bejar, E. Dhahri, M.F.P. Graça, L.C. Costa, Journal of Alloys and Compounds , 2015, 653, 506.

[12] N. Gayathri, A. K. Raychaudhuri, S. K. Tiwary, R. Gundakaram, Anthony Arulraj, C. N. R. Rao, Phys. Rev. B , 1997,56, 1345.

[13] H.Rahmouni, B. Cherif, M. Baazaoui, K. Khirouni, J. Alloys Compd, 2013, 575, 59.

[14] P. D. Battle, T. C. Gibb, P. Lightfoot and M. Matsuo, J. Solid State Chem, 1990, 85, 38

[15] K. S. Roh, K. H. Ryu, C. H. Yo, Journal of Materials Science , 1995, 30, 1245

[16] R.A. Young, The Rietveld Method, International Union of Crystallography & Oxford University Press, New York, 1996.

[17] A. Guinier, in: X. Dunod (Ed.), Théorie et technique de la Radiocristallographie, p.462, 3rd ed, 1964.

[18]H. Khelifi, I. Zouari, A. Al-Hajry, N. Abdelmoula, D. Mezzane, H. Khemakhem, Ceramics. International, 2015, 41, 12958.

[19] P.C. Sati, M. Arora, S. Chauhan, M. Kumar, S. Chhoker, Ceramics. nternational, 2014, 40, 7805.

[20] I. Coondooa, N. Panwarb, M. A. Rafiq, V. S. Pulid, M. N. Rafiqe, R. S. Katiyarf, Ceramics International ,2014, 40 , 9895.

[21] D.C. Sinclair, A.R.West , J.Appl.Phys, 1989, 66, 3850.

[22] A. Benali, A. Souissi, M. Bejar, E. Dhahri, M.F.P. Graça, M.A. Valente, Chemical Physics Letters , 2015, 637, 7.

View Article Online
DOI: 10.1039/C6RA10589K

[23] A.BenHafsia, N.Rammehb, M.Farid, M.Khitounia, Ceramics.International, 2016, 42, 3673.

[24] P.B. Macedo, C.T. Moynihan, N.L. Laberge, Phys. Chem. Glasses , 1973,14, 122.

[25] M. HajLakhdar , T.Larbi, B.Ouni, M.Amlouk, Materials Science in Semi conductor Processing, 2015, 40, 596.

[26] C.T. Moynihan, L.P. Boesch, N.L. Laberge, Phys. Chem. Glasses, (1973), 14, 122.

[27] R. Bergman, J. Appl. Phys , 2000, 88, 1356.

[28] Ridha Bellouz, Sami Kallel , Kamel Khirouni , Octavio Penac, Mohamed Oumezzinea , Ceramics International , 41, 2015, 1929.

[29] Eiki Niwa , Hiroki Maeda , Chie Uematsu , Takuya Hashimoto, Materials Research Bulletin , 2015, 70, 241.

[30] Shahid Husain, Irshad Bhat, WasiKhan, Lila Al-Khataby, Solid State Communications 2013, 157, 29.

[31] M. Dult, R.S. Kundu, S.Murugavel, R. Punia, N. Kishore, Phys. B, (2014), 452, 102.

[32] A. Banerjee, S. Pal, and B. K. Chaudhuri, J. Chem. Phys, 2001, 115, 1550.

[33] A. Banerjee, S. Pal, S. Bhattacharya, B. K. Chaudhuri, and H. D. Yang, Phys. Rev. B , 2001, 64, 104428.

[34] R. C. Devlin, A. L. Krick, R. J. Sichel-Tissot, Y. J. Xie, and S. J. May , J. Appl. Phys , 2014, 115, 233704.

[35] S. Nasri, M. Megdiche, M. Gargouri,Ceramics.International, 2016, 42, 943.

[36] M. Ben Bechir, K. Karoui, M. Tabellout, K. Guidara, A. Ben Rhaiem , J. Appl. Phys. 2014, 115, 153708.

View Article Online
DOI: 10.1039/C6RA10589K

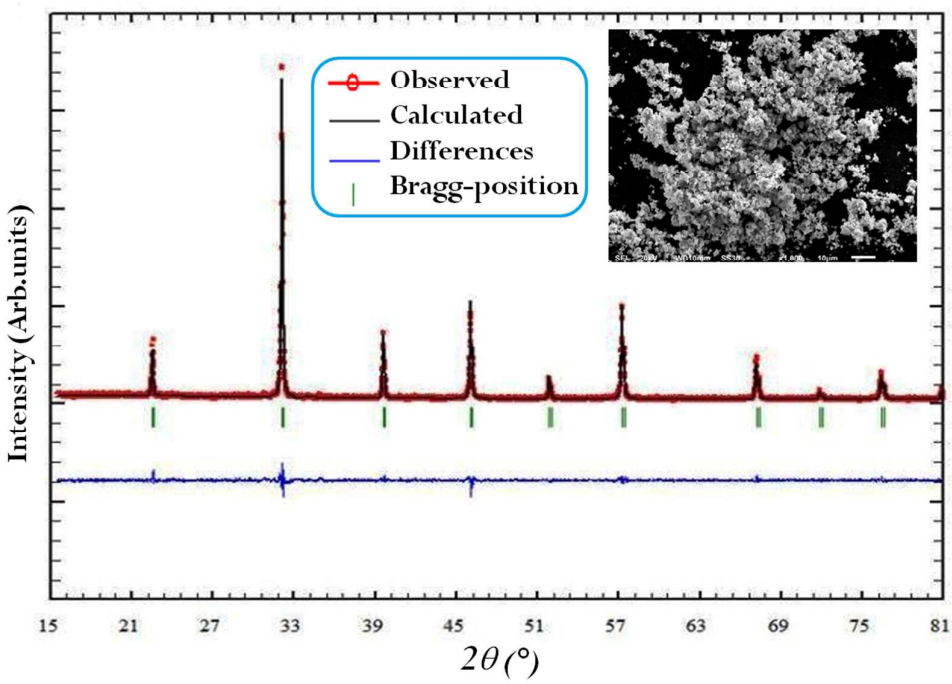

Fig.1

View Article Online
DOI: 10.1039/C6RA10589K

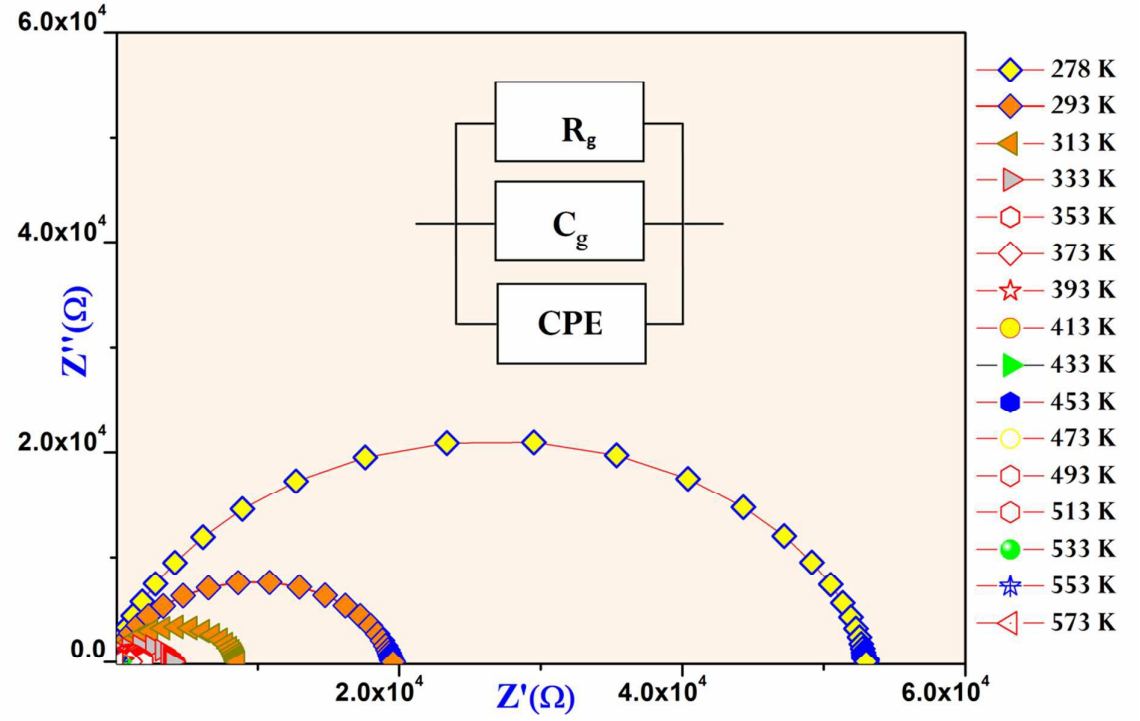

Fig.2

View Article Online
DOI: 10.1039/C6RA10589K

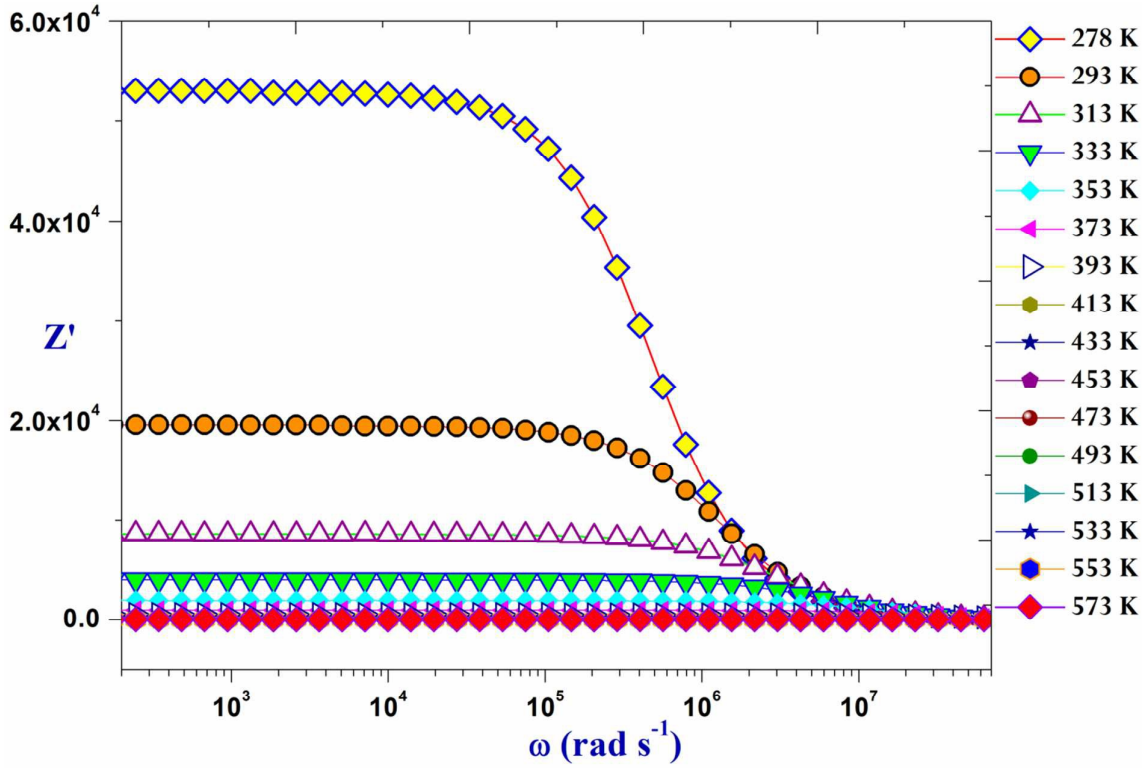

Fig.3

View Article Online
DOI: 10.1039/C6RA10589K

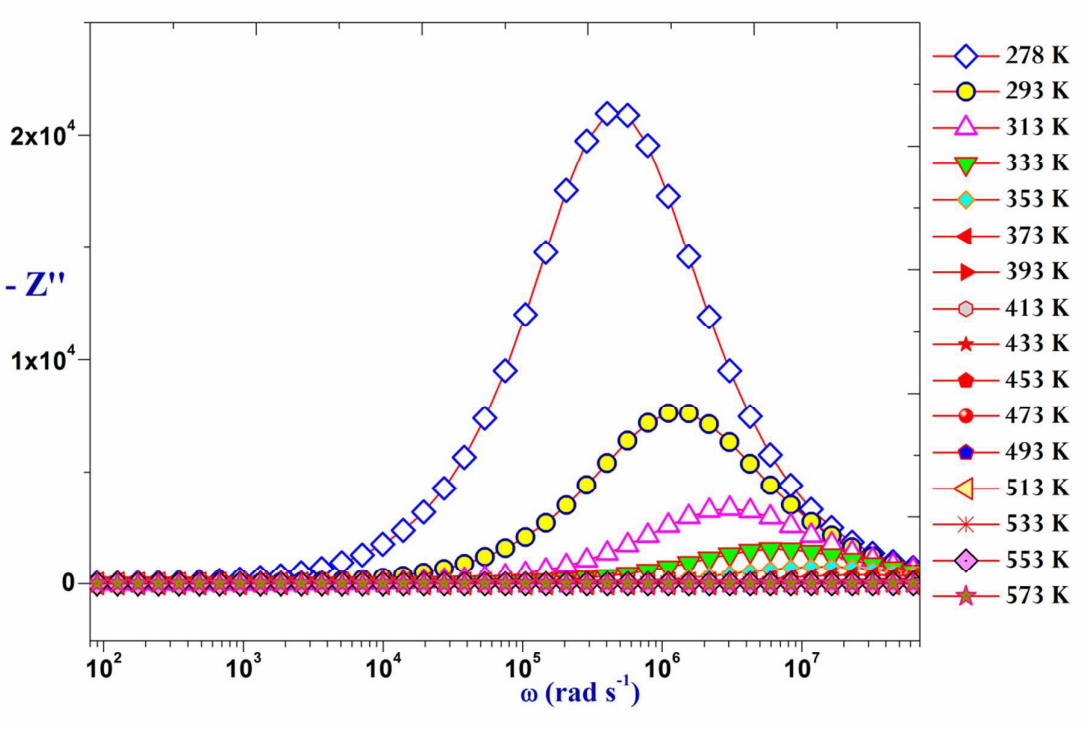

Fig.4

View Article Online
DOI: 10.1039/C6RA10589K

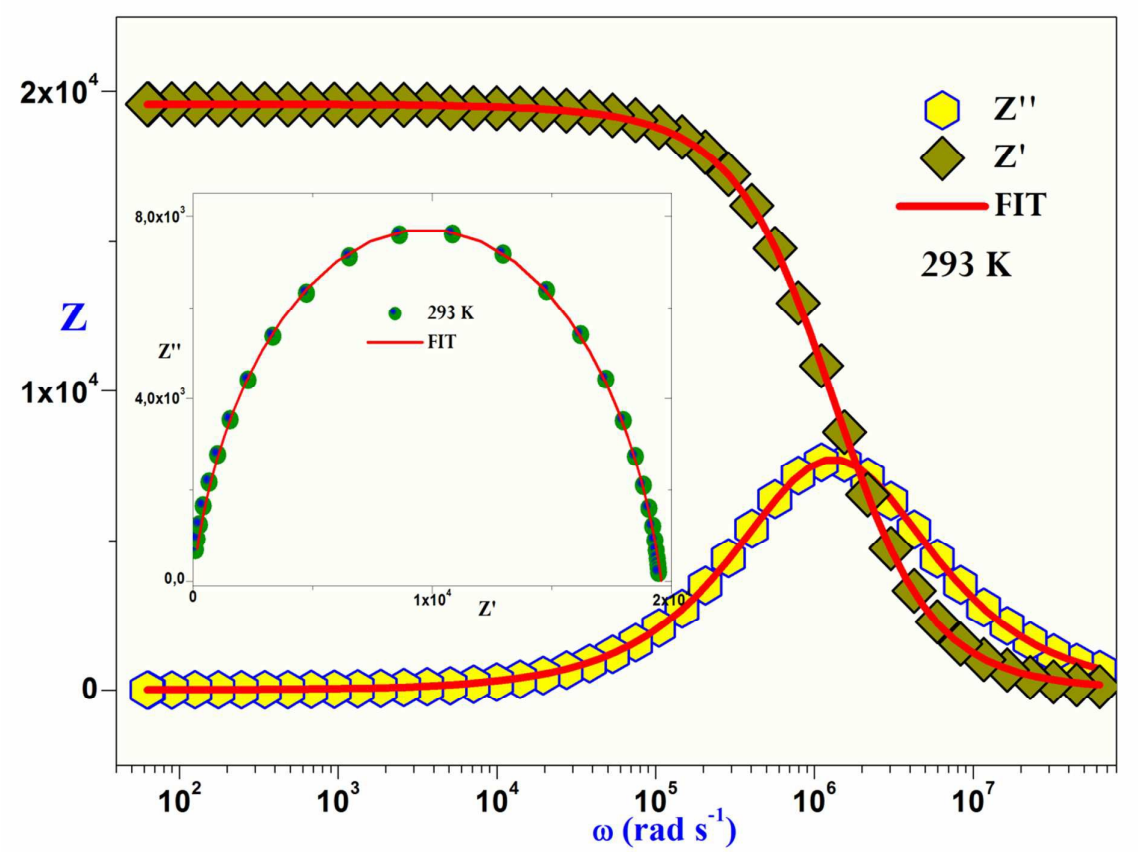

Fig.5

View Article Online
DOI: 10.1039/C6RA10589K

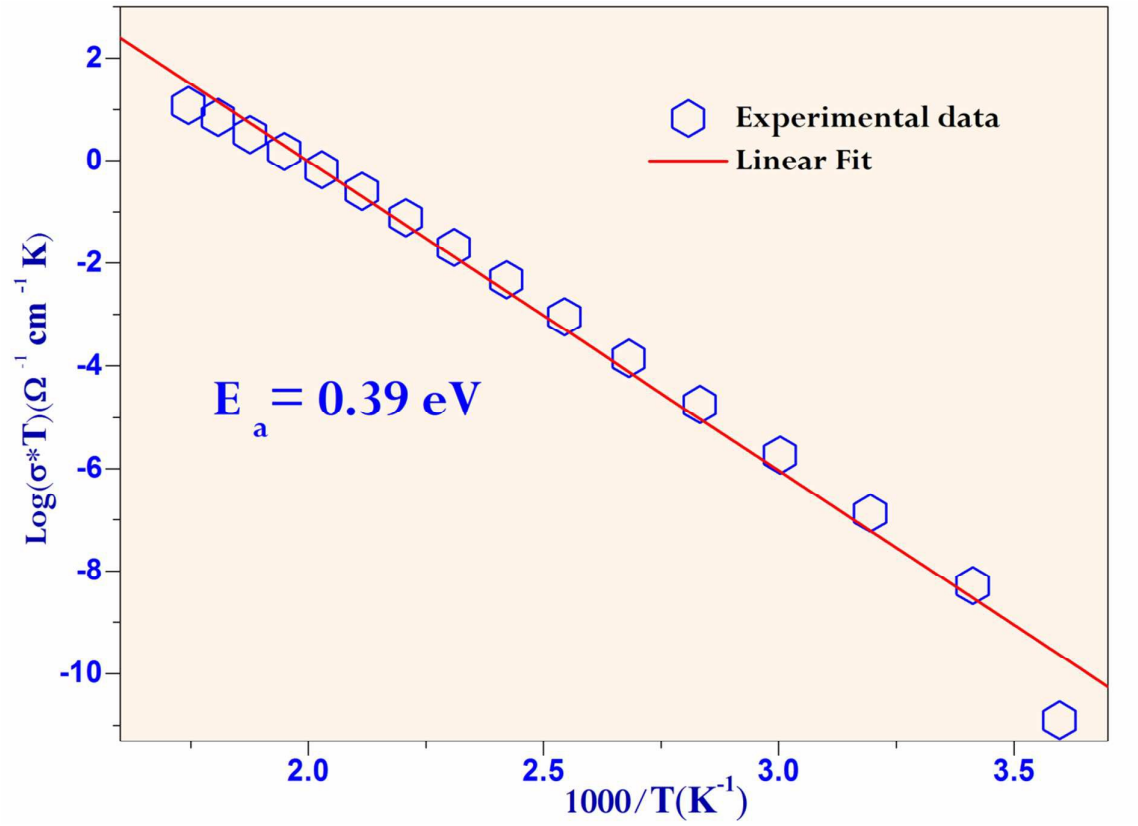

Fig.6

View Article Online
DOI: 10.1039/C6RA10589K

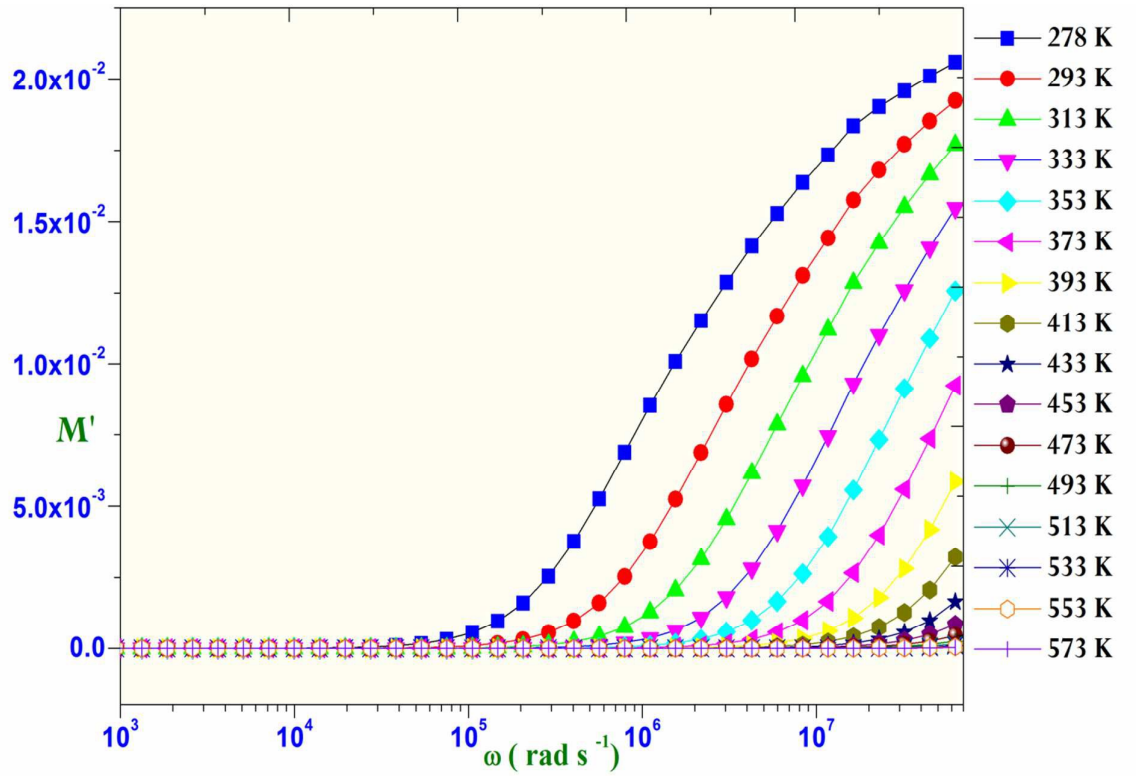

Fig.7

View Article Online
DOI: 10.1039/C6RA10589K

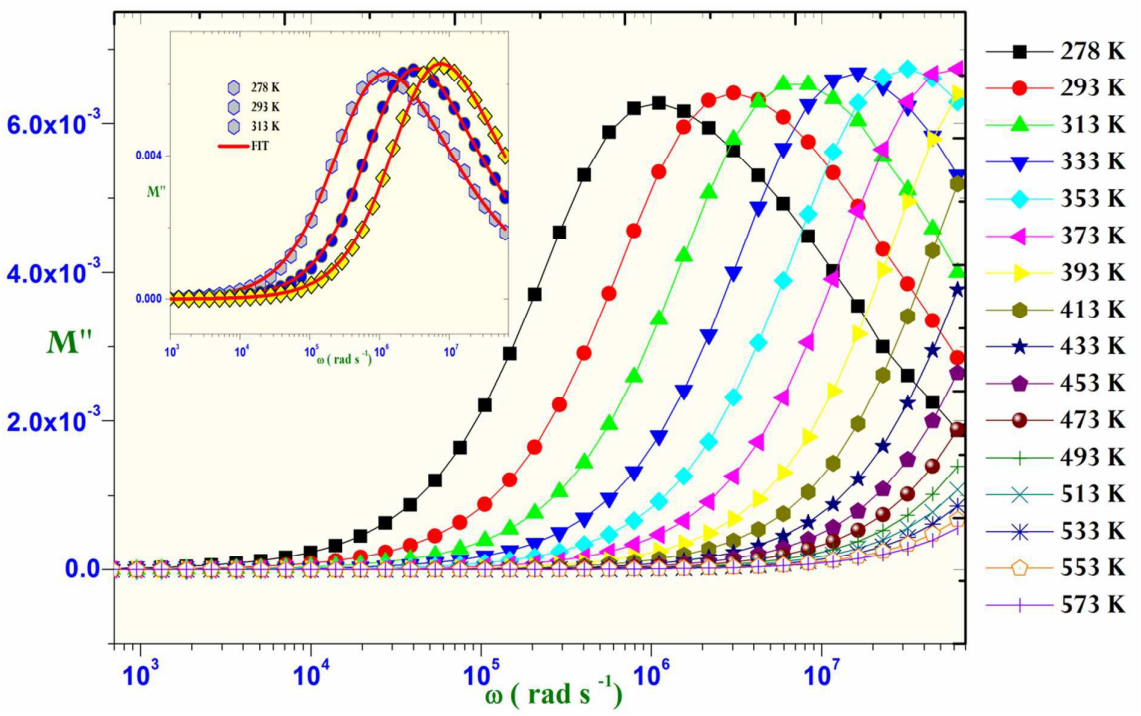

Fig.8

View Article Online
DOI: 10.1039/C6RA10589K

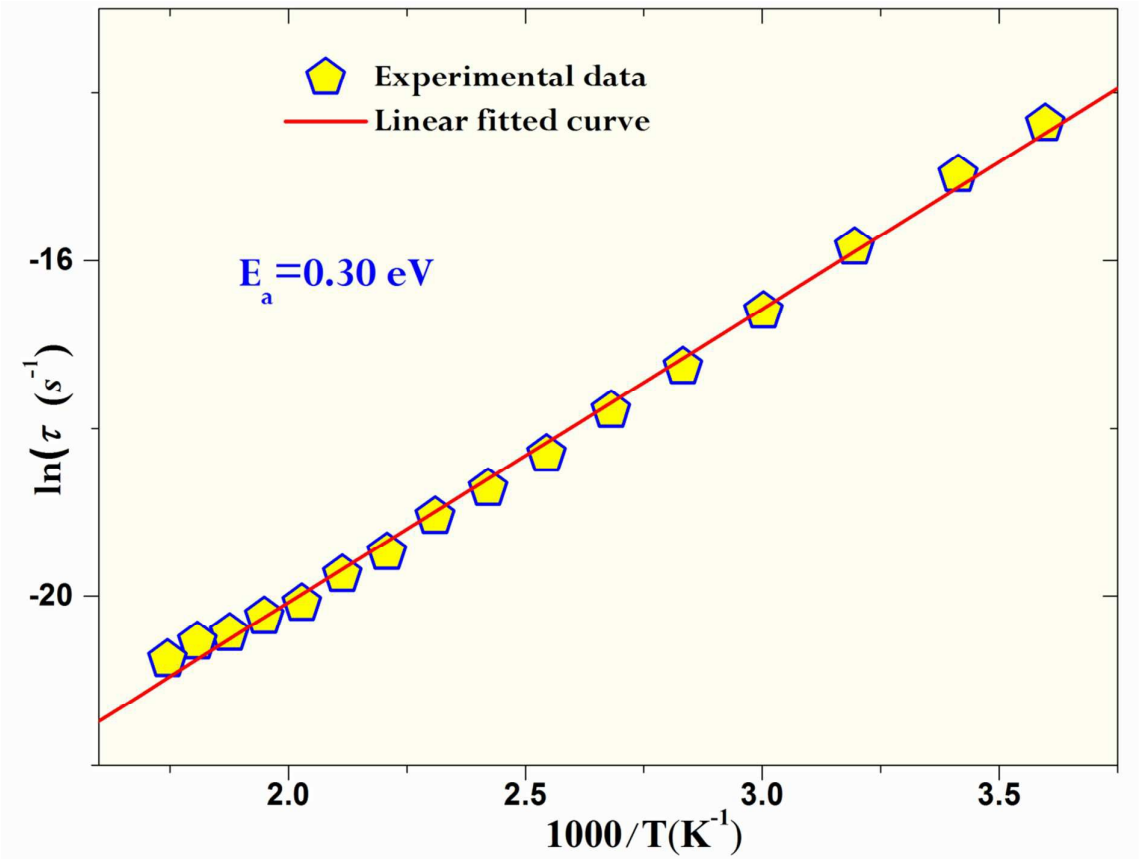

Fig.9

View Article Online
DOI: 10.1039/C6RA10589K

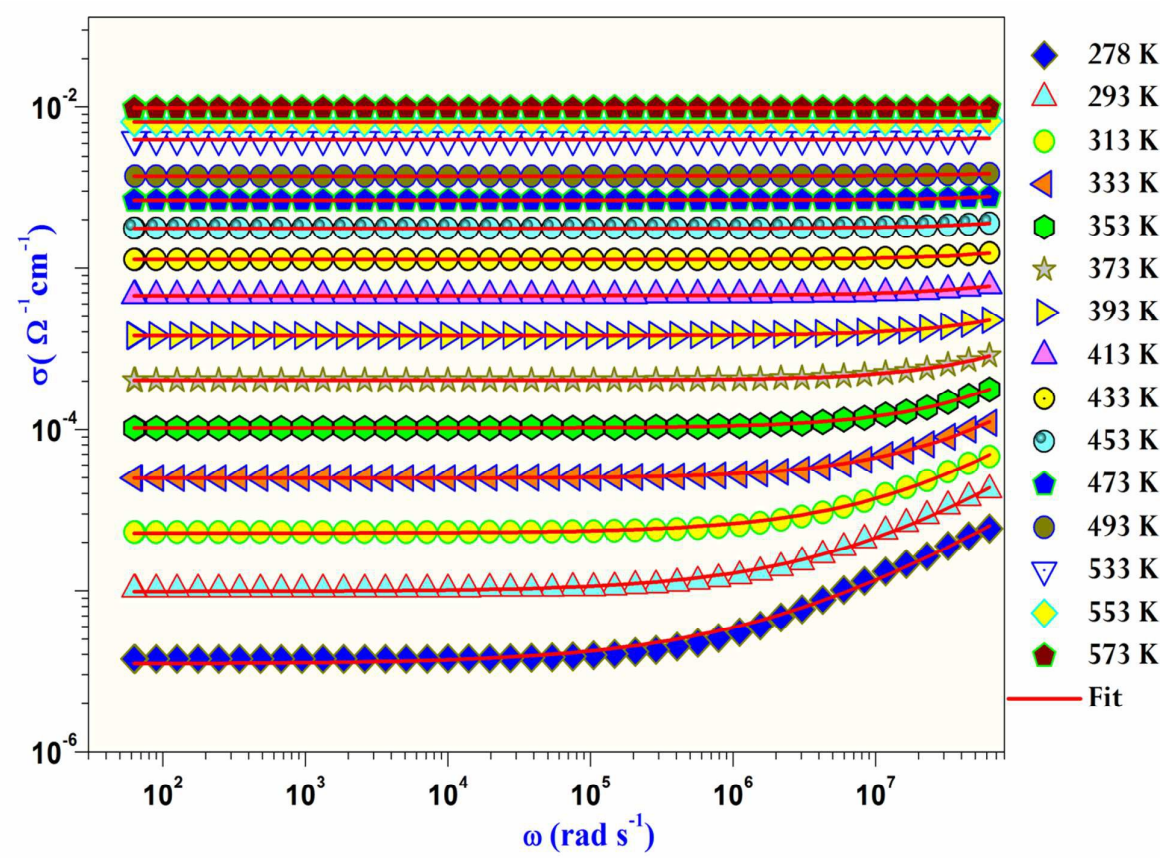

Fig.10

View Article Online
DOI: 10.1039/C6RA10589K

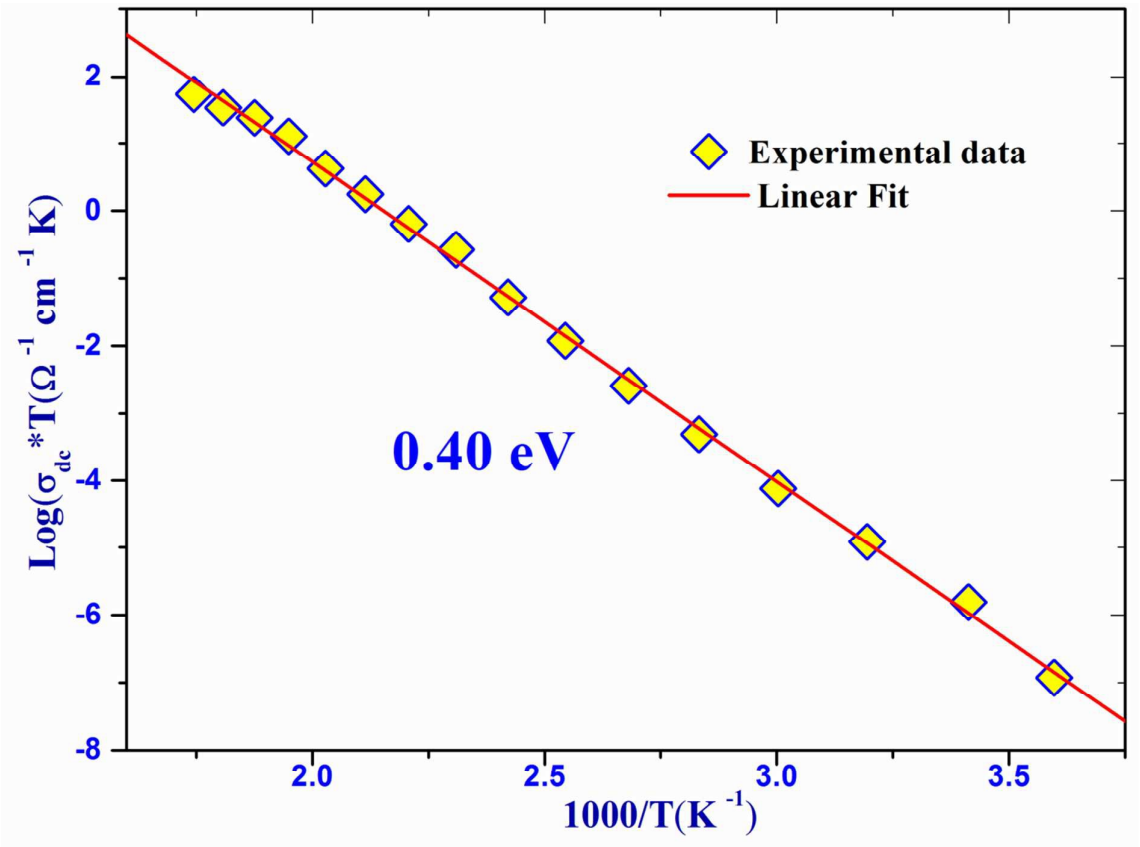

Fig.11

View Article Online
DOI: 10.1039/C6RA10589K

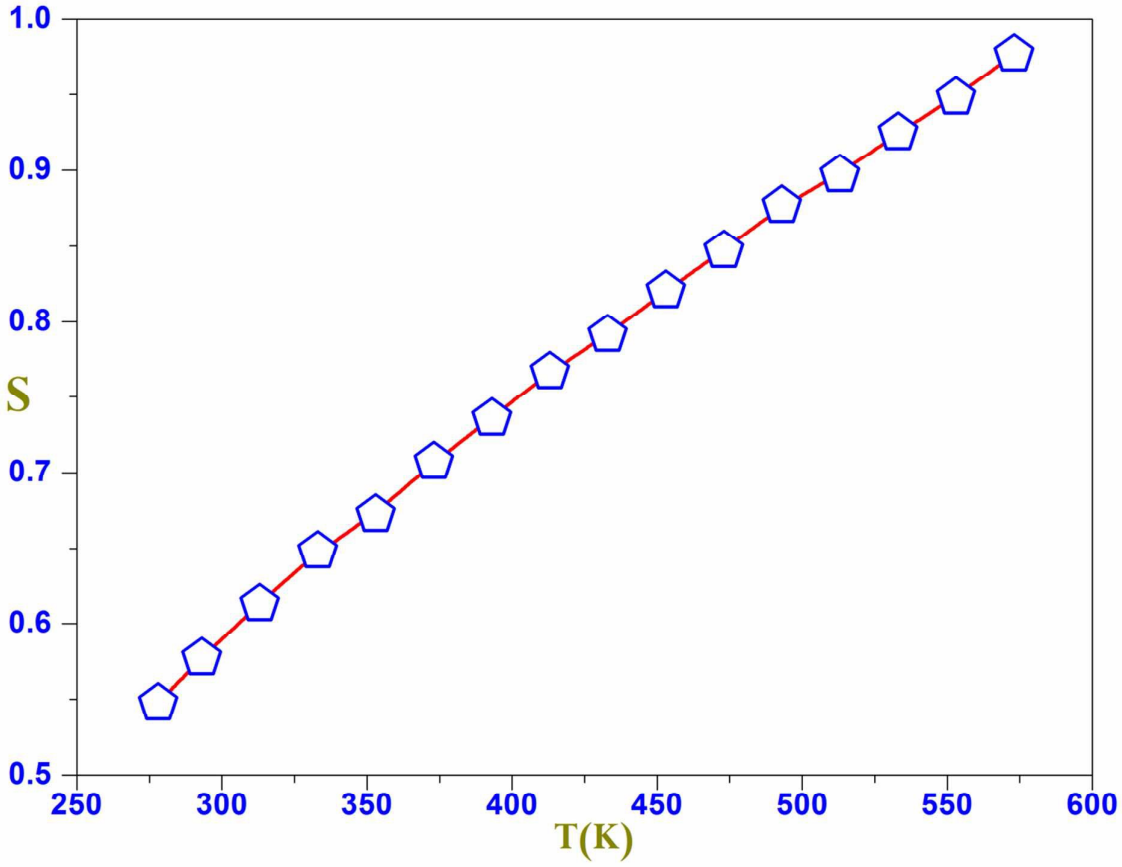

Fig.12

View Article Online
DOI: 10.1039/C6RA10589K

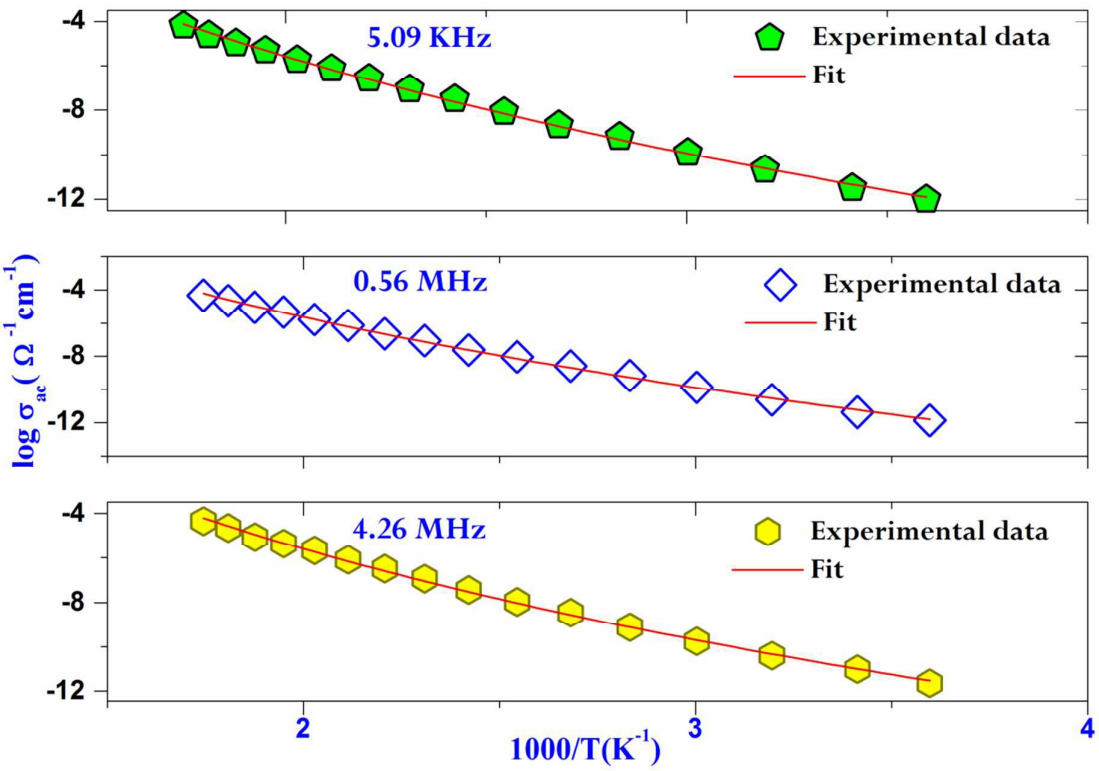

Fig.13

View Article Online
DOI: 10.1039/C6RA10589K

T(K)	σ_{dc} (Ω^{-1} cm^{-1})	A	Exponent S
278	3.53E-06	1.574E-09	0.53
293	1.02E-05	1.529E-09	0.58
313	2.34E-05	9.402E-10	0.64
333	4.87E-05	3.738E-10	0.71
353	1.04E-04	2.384E-10	0.76
373	2.02E-04	1.656E-10	0.79
393	3.72E-04	1.871E-10	0.80
413	6.72E-04	1.717E-10	0.82
433	1.30E-03	7.612E-11	0.88
453	1.82E-03	6.630E-11	0.89
473	2.70E-03	5.187E-11	0.90
493	3.80E-03	4.512E-11	0.91
513	5.90E-03	3.874E-11	0.92
533	7.50E-03	3.064E-11	0.93
553	8.40E-03	1.787E-11	0.95
573	9.90E-03	1.319E-11	0.96

Table.1

	Frequency	α ($Å^{-1}$)	$N(E_F)$ (eV^{-1} cm^{-1})	W_H (eV)
$La_{0.5}Ba_{0.5}FeO_{3-\delta}$	4.26 MHz	1.39	$3.4\ 10^{41}$	0.111
	0.56 MHz	1.24	$5.4\ 10^{39}$	0.145
	5.09 KHz	1.19	3.7610^{37}	0.212

Table.2